Synthesis of Ni–TiO₂ Nanocomposites as Enzyme–less, Amperometric Sensors for the Electrooxidation of Glucose

JP de los Rios, Vicente Galvan, G. K. Surya Prakash*

Loker Hydrocarbon Research Institute, Department of Chemistry, University of Southern California, 837 Bloom Walk, Los Angeles, California 90089, United States

*E-mail: gprakash@usc.edu

DOI 10.1149/2754-2734/acd404

Abstract

The simple synthesis of a Ni–TiO₂ nanocomposite supported on Vulcan carbon (XC–72R) for the electrooxidation reaction of glucose is reported. Four transition metal weight ratios were synthesized and characterized. Cyclic voltammetry studies in 0.1 M NaOH demonstrate that the four metal catalysts can effectively oxidize 1 mM glucose, with the 3:1 (60%) Ni to Ti nanocomposite yielding the highest current. The 60% Ni-TiO₂/XC72R catalyst was used to construct an enzyme-less, chronoamperometric sensor for glucose detection in an alkaline medium. Using 50 µM aliquots of glucose at a potential of +0.7V (vs Hg/HgO), the sensor responded rapidly (< 3 s), provided a sensitivity of 3300 µA mM⁻¹ cm⁻², detection limits of 144 nM (S/N = 3), and excellent selectivity and reproducibility. The glucose aliquot concentrations were then increased to 1 mM to mimic physiological blood conditions of 1–20 mM. At a potential of +0.7V (vs Hg/HgO), the sensor continued to respond rapidly (< 1 s), showed a sensitivity of 273.7 μ A mM⁻¹ cm⁻², detection limits of 3.13 μ M (S/N = 3), and excellent selectivity and reproducibility. The catalyst also exhibited an ideal anti-poisoning capability to free chloride ions and negligible signals towards other interfering species.

1

Introduction

In 1994, The Centers for Disease Control and Prevention declared that diabetes had reached epidemic proportions. Since then, however, little has been done to suppress the yearly increasing statistics. As of 2019, global diabetes prevalence reached 463 million people (9.3%) and it is expected that by 2045, an astounding 700 million people (10.9%) worldwide will be diagnosed with this condition. Studies throughout the 2020 coronavirus (COVID–19) pandemic demonstrated that older age and presence of diabetes mellitus, hypertension, and obesity significantly increased the risk for hospitalization and death in COVID–19 patients. Presently, a positive diabetes diagnosis undoubtedly diminishes an individual's health and quality and duration of life. Efforts should focus on both raising awareness at a global scale and developing preventive measures and effective treatments as part of fundamental care and health. Reliable sensors for monitoring glucose levels continue to be of major importance for diabetes control and treatment.

Enzymatic biosensors with incorporated transductors, specifically glucose oxidase biosensors, have been studied and developed extensively for this mission. Despite their low detection limit and high selectivity, enzymatic biosensors often require complex immobilization techniques of the enzyme onto a substrate electrode and often suffer from leakage and poor stability. Glucose oxidase biosensors can also only work properly under specific temperatures, pHs, and chemical environments. Alternatively, nonenzymatic amperometric biosensors continue to be investigated as potential substitutes to enzymatic biosensors. Previous literature has focused on the development of nanostructured metals [12–14], metal alloys [9,15–18], and metal oxides [19–23] as electrocatalytic materials for glucose oxidation. Many of these materials display faster response times, lower detection limits, and better stability compared to enzymatic biosensors. However,

their selectivity towards other carbohydrates besides glucose are often discernable and they can suffer from poisoning by intermediates and other ions.^[23,24]

Electrochemical oxidation of glucose has been demonstrated to be enhanced by nickel catalysts given the existence of the Ni(OH)₂/NiOOH (Ni²⁺/Ni³⁺) redox couple in an alkaline medium.[13] Nickel's popularity stems from its spontaneous transformation into NiO, which consequently forms Ni(OH)₂ due to adsorption of hydroxide ions.^[12] At specific potentials, the Ni(OH)₂ is converted to NiOOH, which is the active form for the electrooxidation of glucose.^[25] Nickel is also an abundant, nontoxic, inexpensive metal demonstrating commercial and industrial applicability. Continually, the incorporation of transition metal oxides as substrates for catalysis is common in the field of chemical sensors. Specifically, TiO₂ has been widely studied as a substrate for chemical sensors due to its multiple morphologies, biocompatibility, nontoxicity, and chemical and thermal stability. It's classification as an n-type semiconductor improves the transport of surface reaction electrons to the metal substrate. [26] This ultimately enhances the performance of the sensor. Previous studies have examined the synergistic effects of nickel and titanium for the oxidation of glucose; however, these investigations often employ complex morphologies that require more elaborate synthetic methods.^[25,27,28] Herein we expand on prior work by presenting a simple chemical reduction of Ni nanoparticles unto a TiO₂ anatase substrate with Vulcan carbon for the development of a nonenzymatic sensor for glucose electrooxidation. Multiple wt. % of Ni and TiO₂ were investigated to optimize the ratio of the chemical species that would be the most active towards the oxidation reaction. The two linear ranges of 50 μM–1 mM and 1-20 mM glucose demonstrated a versatile sensor with exceptional response times and selectivity. Our studies using a nanocomposite of 60% Ni on 20% TiO₂ as an anode electrode reports the highest sensitivity of 3300 µA mM⁻¹ cm⁻² with the lowest detection limit of 144 nM.

Materials and Methods

Chemicals. – Ni(NO₃)₂ · 6H₂O (99.9% purity) was purchased from Strem Chemicals, anatase TiO₂ catalyst support (1/8" pellets) was purchased from Alfa Aesar, D–Glucose Anhydrous (granular) purchased from Macron Chemicals, Vulcan carbon (XC–72R) and 5% Nafion binder solution were purchased FuelCell store. Analytes were used as received without further purification: L–ascorbic acid sodium salt (99%) purchased from Alfa Aesar, DL–lactic acid purchased from Sigma Aldrich, and uric acid purchased from Strem Chemicals. Millipore water (18.2MΩ cm) was used for all solution preparations. All other reagents were of analytical grade and used without further purification. The electrochemical measurements were performed in 0.10 M NaOH solution.

*Preparation of Ni–TiO*₂/XC72R catalyst.— To synthesize the 60% Ni–TiO₂/XC72R catalyst, 297.3 mg Ni(NO₃)₂ · 6H₂O and 33.4 mg anatase TiO₂ were dispersed in 20 mL ethylene glycol. Then 20.0 mg of Vulcan carbon XC–72R was added into the solution and stirred for 30 min followed by slow addition of 936 μL of 35% hydrazine hydrate. The solution was stirred for an additional 30 min. The mixture was transferred to a Teflon lined vessel and heated to 150 °C for 6 h in an oven. After the 6 h had elapsed, the solution was transferred to a centrifuge tube and 20 mL of DI H₂O were added. The solution was centrifuged at 6000 rpm for 5 min and the supernatant was discarded. The washing process was repeated two additional times with water and finally dried in oven for 24 h at 60 °C resulting in a black powder. Similar syntheses were completed but varying the weight ratios 1:3 (20%), 1:1 (40%), and 4:0 (80%) of Ni:Ti.

Electrochemical testing.– The electrode system consisted of a glassy carbon (GC) rotating disk electrode (RDE) with a geometric surface area of 0.195 cm² attached to a Pine Research MSR Rotator, 4.24 M KOH Hg/HgO (MMO) reference electrode, and Pt wire counter electrode. Prior to any measurements the GC RDE was polished with a microcloth and 0.05 μm alumina slurry

bought from Electron Microscopy Sciences. All voltammetric determinations were carried out with a Solartron Analytical 1287A Electrochemical Interface potentiostat/galvanostat instrument. The electrochemical measurements were performed in 0.10 M NaOH solution and 1 mM glucose. Nitrogen gas was flushed for 30 min prior to experiments and steadily flowed during all voltammetric measurements. Catalyst inks were obtained by dissolving 2.5 mg of dried catalyst and 7.5 mg (\sim 10 μ L) of 5% binder into 100 μ L isopropanol/900 μ L DI H₂O mixture. The solution was sonicated for 24 min. Then 20 μ L of the catalyst ink was dropcast unto the GC RDE and dried in an oven at 60 °C for 30 min. All electrochemical experiments were normalized to the geometric surface area of the GC RDE.

Physical characterization.– Powder X–ray diffraction (XRD) measurements were performed on a Rigaku Ultima IV X–ray diffractometer with Cu Kα (0.154056 nm) radiation source and a scan rate of 6° min⁻¹ from a 2Θ value of 10° to 90°. Scanning electron microscopy (SEM) images were obtained from a Nova NanoSEM 450 field emission scanning electron microscope with an acceleration voltage of 18.0 keV. Energy dispersive X–ray spectroscopy (EDS) measurements were conducted in a JSM 7001F Field Emission Scanning Electron Microscope. Inductively Coupled Plasma Optical Emission Spectroscopy (ICP–OES) measurements were conducted in a Thermo Scientific iCAP 7400 ICP–OES Analyzer monitoring both Ni spectral lines of 221.647 nm and 231.604 nm. X–ray Photoelectron spectroscopy (XPS) spectra were collected on a Kratos Axis Ultra DLD using a mono Al anode with a pass energy of 160 keV for the survey scan and 20 keV for the high–resolution scans.

Results & Discussion

Physical characterization.— The four nanocomposites, with varying nickel to titania wt. %,were first synthesized and characterized by SEM. Figure 1a demonstrates the SEM image for the 60%

Ni–TiO₂/XC72R catalyst. Figures 1b shows an SEM image and the energy–dispersive spectroscopy (EDS) mapping for this nanocomposite. It is observable from the mapping images that the material is composed of Ti, Ni, O, and C only. The SEM images and corresponding EDS mapping images are demonstrated in Figures S1a–1c for the 20% Ni–TiO₂/XC72R, 40% Ni–TiO₂/XC72R, and 80% Ni/XC72R, respectively. The EDS spectrums in Figures S2a–S2d show the signals for all constituent elements and their corresponding wt. % in the Ni–TiO₂/XC72R nanocomposites without any other impurities present. According to EDS, the nickel content in the

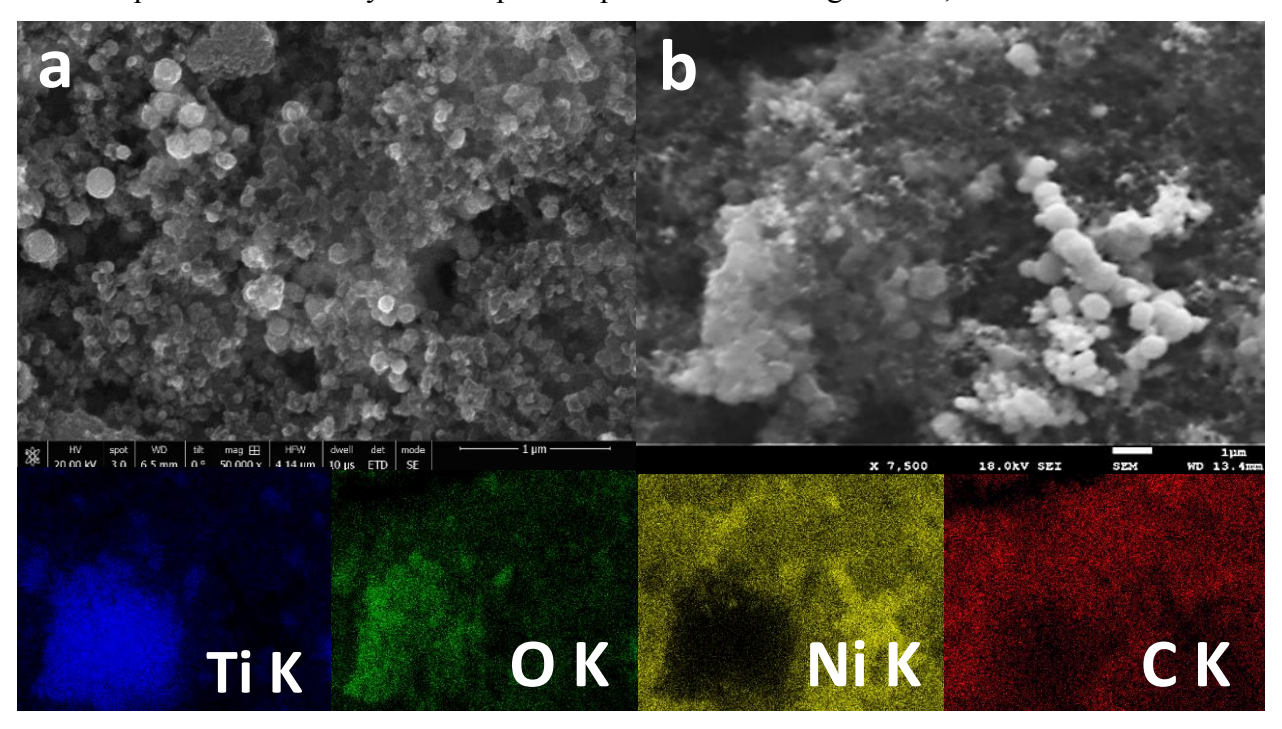


Figure 1. (a) SEM image of the 60% Ni–TiO₂/XC72R nanocomposite and (b) EDS elemental mapping of the 60% Ni–TiO₂/XC72R nanocomposite.

20% Ni–TiO₂/XC72R, 40% Ni–TiO₂/XC72R, 60% Ni–TiO₂/XC72R, and 80% Ni/XC72R nanocomposites were 24.02%, 45.30%, 58.48%, and 80.60%, respectively. Inductively Coupled Plasma Optical Emission Spectroscopy (ICP–OES) measurements were conducted to further quantify the Ni content in the synthesized nanocomposites. Solutions of 55 ppm in 2% HNO₃ were prepared for each of the four nanocomposites and the Ni spectral lines of 221.647 nm and 231.604 nm were selected. Figure S3 demonstrates that, as expected, the nickel loading increased

analogously to the incrementing nickel–to–titania ratio for both spectral lines. The nickel loading in the nanocomposites referencing the 221.647 nm and 231.604 nm spectral lines respectively were determined to be 16.89% and 19.06% for the the 20% Ni–TiO₂/XC72R, 39.03% and 41.11% for the 40% Ni–TiO₂/XC72R, 58.99% and 60.86% for the 60% Ni–TiO₂/XC72R, and 77.63% and 79.34% for the 80% Ni/XC72R.

XRD measurements were conducted to obtain the catalysts' crystallographic data and confirm the formation of a Ni–TiO₂ nanocomposite with varying metal ratios. The XRD patterns in Figure S4 shows reflections for Ni nanoparticles (*) on an anatase TiO₂ substrate (‡). The peaks with 20 values of 44.59°, 51.91°, and 76.49° correspond to the (1 1 1), (2 0 0), and (2 2 0) planes in nickel nanoparticles, respectively. [29] Whereas, the peaks corresponding to TiO₂ anatase are given at 20 of 25.44°, 37.10°, 44.59°, 54.00°, 55.18°, 62.81°, 68.91°, 70.40°, 75.17°, 76.22°, and 82.82°. [30] As the titania wt. % decreases and more nickel is incorporated into the catalysts, the intensity from the titania reflections diminish until eventually disappearing at the 80% Ni/XC72R catalyst and those from the nickel nanoparticles become more apparent. As expected, the 20% Ni-TiO₂/XC72R nanocomposite displays the lowest intensity for the Ni nanoparticle reflections and the highest for the TiO₂ substrate. Furthemore, the nickel crystallite size increases as the wt. % of TiO₂ decreases in the catalysts. The average crystallize size of the catalysts was calculated using the Debye-Scherrer equation and the broadening of the (1 1 1) peak. The average crystallite size for the 20% Ni-TiO₂/XC72R, 40% Ni-TiO₂/XC72R, 60% Ni-TiO₂/XC72R, and 80% Ni/XC72R were determined to be 9, 11, 12, and 13 nm, respectively. The nanocomposites were then characterized through XPS in order to understand the surface compositions.

XPS wide scans are shown in Figure S5. The four different nanocomposites show the presence of only the expected elements. Carbon, oxygen, and nickel signals are revealed in all the samples

while titanium cannot be observed in the 80% Ni/XC72R nanocomposite, as expected. These XPS survey scans help validate the presence of titania at the surface of the nanocomposites except for the 80% Ni/XC72R catalyst. Furthermore, the nickel wt. % in each nanocomposite surface were determined from the survey scans, shown in Table S1. The 20% Ni–TiO₂, 40% Ni–TiO₂, 60% Ni–TiO₂, and 80% Ni/XC72R nanocomposites had wt. % of 11.93%, 16.58%, 21.13%, and 34.63%, respectively. These values are lower compared to the EDS data given that the penetration depth of the XPS electron beam occurs strictly at the surface of the material. Nonetheless, the nickel wt. % at the surface are in accordance with the expected trend as nickel content is increased in the catalysts. Figure 2a–2d demonstrates the high-resolution scans for the four nanocomposites monitoring the Ni 2p core level. The binding energies of the Ni 2p can be resolved into a doublet

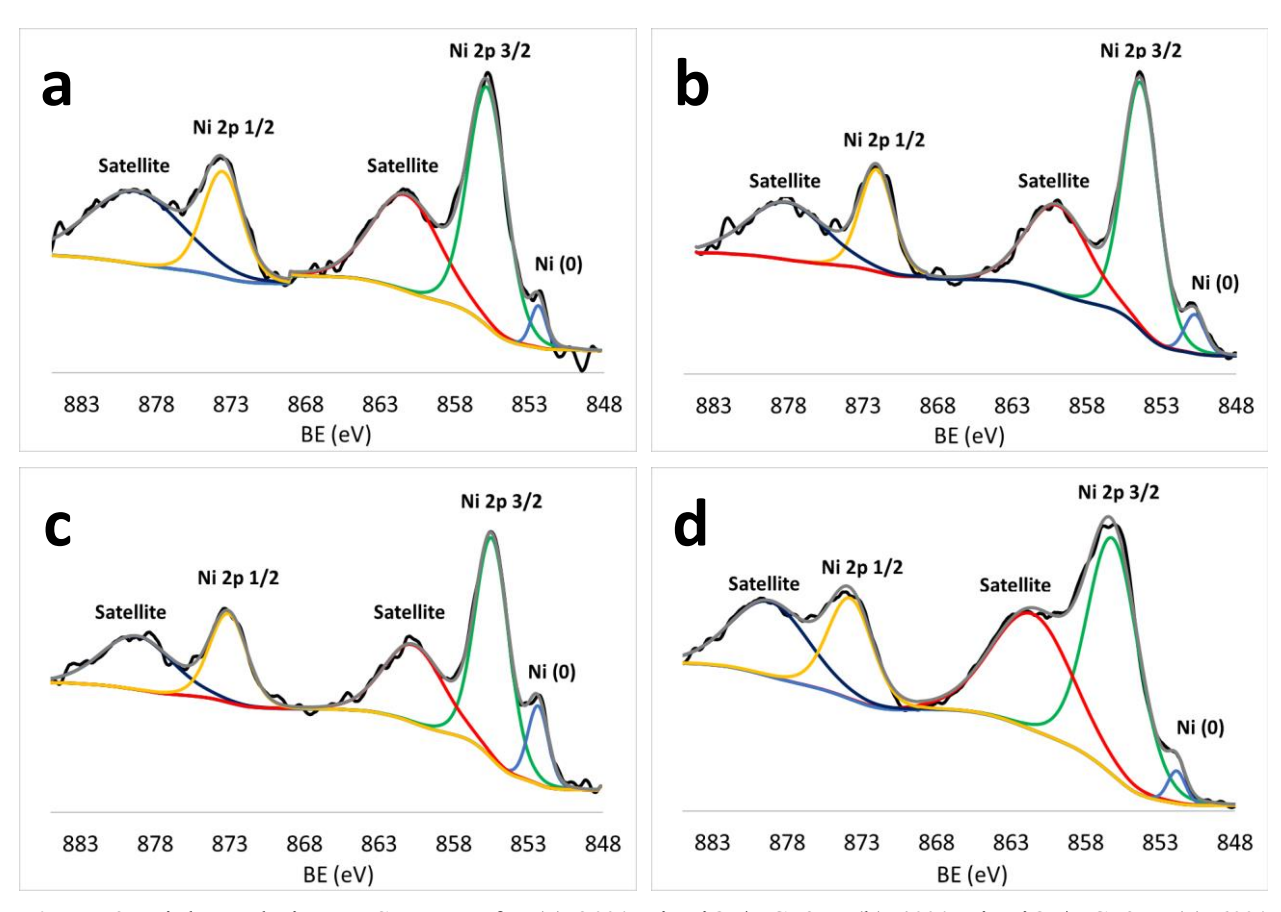


Figure 2. High resolution XPS spectra for (a) 20% Ni–TiO₂/XC72R, (b) 40% Ni–TiO₂/XC72R, (c) 60% Ni–TiO₂/XC72R and (d) 80% Ni/XC72R.

of Ni 2p_{1/2} and Ni 2p_{3/2}, as a result of spin–orbital coupling. The Ni 2p_{3/2} curves are deconvoluted into two regions corresponding to the oxidation states of Ni(II) at 855.5 eV and Ni(0) at 852 eV. Therefore, the high resolution XPS scans can validate the coexistence of Ni(II) and Ni(0) on the surface of the material. The presence of metallic nickel in the 20% Ni–TiO₂, 40% Ni–TiO₂, 60% Ni–TiO₂, and 80% Ni/XC72R are 2.48%, 3.55%, 7.82%, and 1.80%, respectively. This quantification demonstrates that the 80% Ni/XC72R is mostly in the Ni(II) state. It also shows that an increase in titania content in the nanocomposites leads to more nickel nanoparticle formation, with the 60% Ni–TiO₂ having the highest presence at 7.82% Ni(0).

Catalyst activation & stability. - Prior to glucose oxidation measurements, the activation and stability of the synthesized catalysts were investigated. The 60% Ni–TiO₂/XC72R nanocomposite was subjected to activation treatment in 0.1 M NaOH at various potentials by applying a sweep rate of 50 mV/s until the maximum currents were obtained. Figures S6a-S6c demonstrate the activation of the 60% Ni-TiO₂ nanocomposite at different potential windows. Table S2 summarizes these results and shows that widening the potential window leads to more rapid stabilization of the active nickel species by decreasing the number of CV scans. It also demonstrates that higher currents are generated at larger potential windows. Figure 3a displays 8 consecutive CV scans of the 60% Ni–TiO₂/XC72R electrode at +0.9V vs. MMO. The second scan demonstrates the appearance of the cathodic and anodic peaks at 398 mV and 598 mV, respectively. This redox couple can be attributed to the nickel oxidation from Ni²⁺/Ni³⁺. The cathodic peak shifts to more negative potentials and the anodic peak to more positive ones as the cycle numbers are increased. These translations in peak position are due to the changes in the crystal structures of the Ni(OH)2 and NiOOH constituents of the surface film.^[13] The gradual increase in maximum peak height demonstrates the progressive nucleation of NiOOH species from Ni(OH)₂ to form an active layer that stabilizes at 305 mV and 705 mV after just 8 cycles. The remaining 20% Ni–TiO₂, 40% Ni–TiO₂, and 80% Ni nanocomposites were activated in 0.1 M NaOH for 8 cycles as shown in Figures S7a–S7c. From the catalyst activation experiments, it is noticeable that the 60% Ni–TiO₂ yields the highest current density at 8 cycles. This demonstrates that the wt. % ratio of 3:1 nickel–to–titania is the most electrochemically active. To gain further insight into the difference in the observed current, the electrochemical surface area (ECSA) for each catalyst was calculated using the "Beta' method" by integrating the stabilized transition of Ni(II) to Ni(III).^[31] For the 20% Ni–TiO₂ and the 40% Ni–TiO₂ catalysts, the integration was

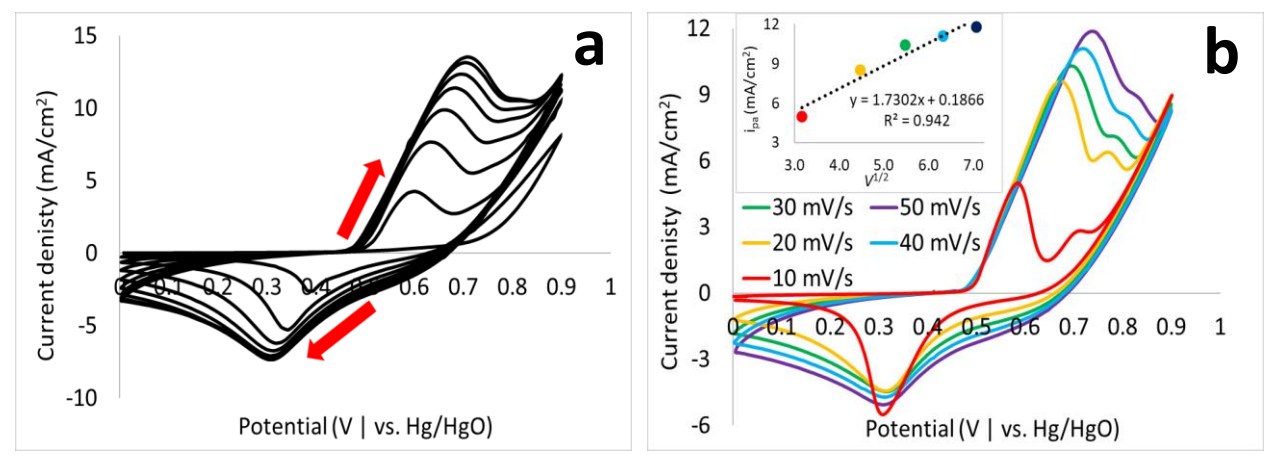


Figure 3. (a) Activation of the 60% Ni–TiO₂/XC72R catalysts (vs. Hg/HgO) in 0.1 M NaOH from 0–+0.9 V at a scan rate of 50 mv/s and (b) at varying scan rates.

calculated in the potential window of +0.5–0.7 V and for the 60% Ni–TiO₂ and the 80% Ni catalysts, the integration was calculated in the potential window of +0.5–0.75 V. The calculated ECSA for the 20% Ni–TiO₂/XC72R, 40% Ni–TiO₂/XC72R, 60% Ni–TiO₂/XC72R, and 80%Ni/XC72R are 97.4 m²/g, 139.04 m²/g, 161.12 m²/g, and 89.44 m²/g, respectively. These values further confirm that the higher current density of the 60% Ni–TiO₂ is a result of increased ECSA.

Furthermore, Figure 3b demonstrates the electrode activation in the potential window from 0–+0.9V at various scan rates. At a potential sweep rate of 10 mV/s two anodic peaks can be

visualized, which become less apparent as the scan rate increases. These peaks demonstrate the distinct nickel phases.^[32] Bode et al. proposed a scheme that involved two phases of nickel hydroxide, α - and β -Ni(OH)₂, and the two phases of the nickel oxyhydroxide species, γ - and β -NiOOH.^[33] The β-Ni(OH)₂ phase has a brucite structure with short interlayer distances of 4.605 Å while the α-Ni(OH)₂ phase is less defined, highly hydrated, and has large interlayer distances (> 8 Å).^[34] Upon electrochemical exposure in base, the β–Ni(OH)₂ phase is oxidized to β–NiOOH while retaining its highly dense, packed structure and the α -Ni(OH)₂ is converted to the γ -NiOOH phase while preserving its disordered and poorly defined configuration. Recent studies, however, have demonstrated that a mixing of the two phases is possible with both long α - and short β interlayer distances coexisting in the material. These materials were first proposed as "badly crystallized β " or β_{bc} . [35] More extensive studies are necessary to decouple the α^{II}/γ^{III} and β^{II}/β^{III} phases given that their presence is nonstoichiometric. Nonetheless, it can be seen from the inset in Figure 3b that plotting the maximum peak current (i_{pa}) vs. square root of the voltage scan rate ($V^{1/2}$) gives a linear relationship. This suggests that the oxidation of Ni(OH)₂ to the NiOOH is a diffusion limited process, which agrees with previous reports. [36] Furthermore, the short–term stability of the Ni-TiO₂/XC72R catalysts at a potential of +0.7V in 0.1 M NaOH is shown in Figure S8. All catalysts demonstrate no loss in current in the tested time period, indicating the overall catalyst stability under the alkaline conditions.

Glucose oxidation.– Figure 4 demonstrates the last activation scan for each electrode in 0.1 M NaOH at a scan rate of 20 mV/s and the subsequent addition of 1 mM glucose. The anodic peaks shift to positive values and are enhanced upon the addition of glucose, indicating an interaction between glucose and the catalyst. Even though all catalysts exhibited electrooxidation of glucose from +0.50–0.75V, the 60% Ni–TiO₂/XC72R catalyst produced the highest activity with a

maximum current density of 9.80 mA/cm². This current density was higher due to the greater wt. % of nickel when compared to the 20% and 40% Ni–TiO₂/XC72R nanocomposites. Additionally, when compared to the 80% Ni/XC72R, the incorporation of titania anatase in the 60% Ni–TiO₂/XC72R plays a significant role. First, it demonstrated that more Ni(0) species are present at the electrode surface, which can spontaneously transform to Ni(III) in alkaline media. Second, it yielded the largest ECSA at 161.12 m²/g, which would allow for more reactivity towards the analyte of interest.

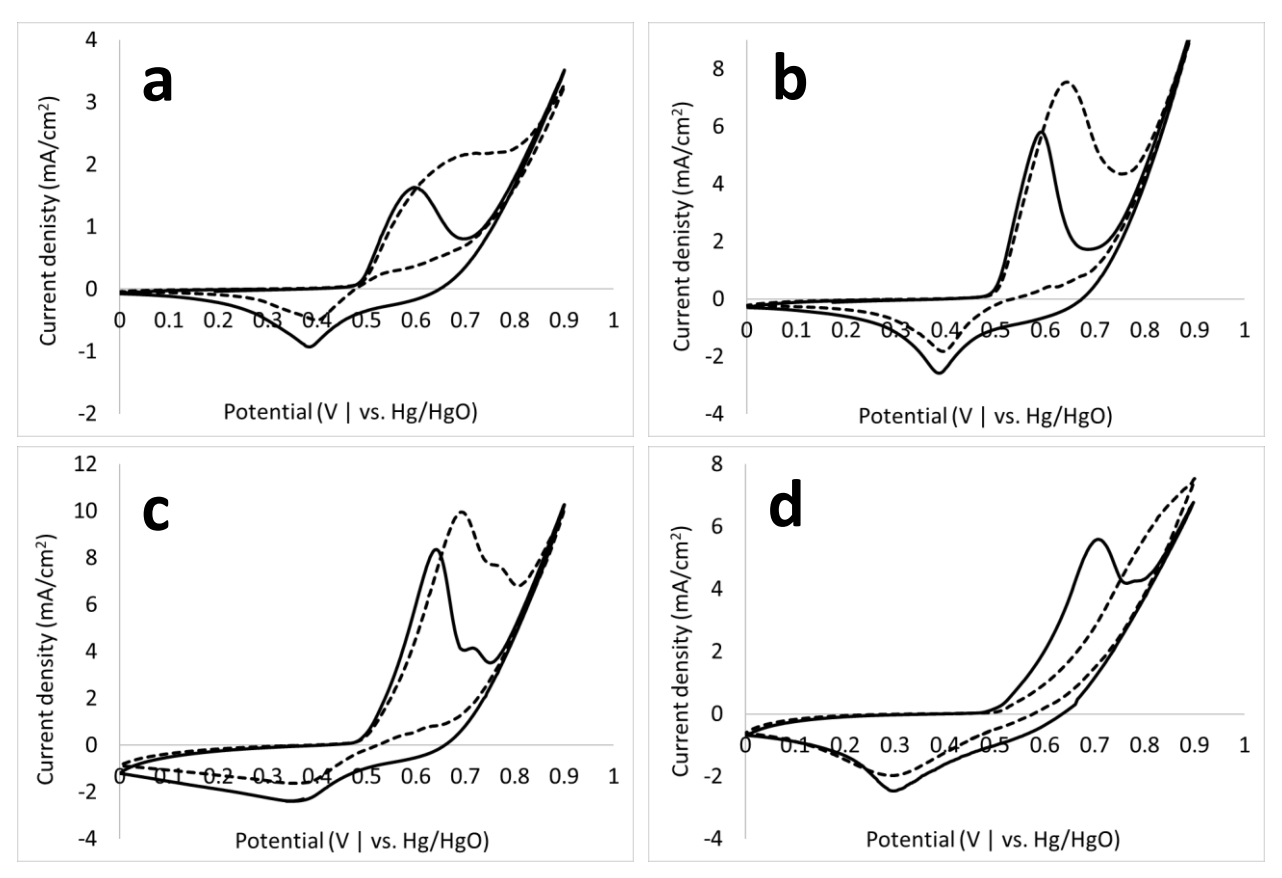


Figure 4. CVs of the Ni–TiO₂/XC72R electrodes (a) 20%, (b) 40%, (c) 60%, and (d) 80% at a scan rate of 20 mV/s in 0.1 M NaOH (solid) + 1 mM glucose (dotted).

Chronoamperometric glucose sensing.— Given the improved catalytic activity of the 60% Ni—TiO₂/XC72R catalyst, chronoamperometric experiments in glucose were conducted at different potentials; shown in Figure 5 with their corresponding calibration curves. Aliquots of 50 μM

glucose were added into the 0.1 M NaOH electrolyte every 50 s while the RDE was rotating at 420 rpm. These aliquot concentrations were selected because the nanocomposite would be applied as the noninvasive alternative for glucose monitoring. This is because statistically significant correlation can be found between blood glucose levels and salivary glucose levels. In a previous study, it was found that patients with blood glucose levels between 100 and 280 mg/dL (5.6 mM

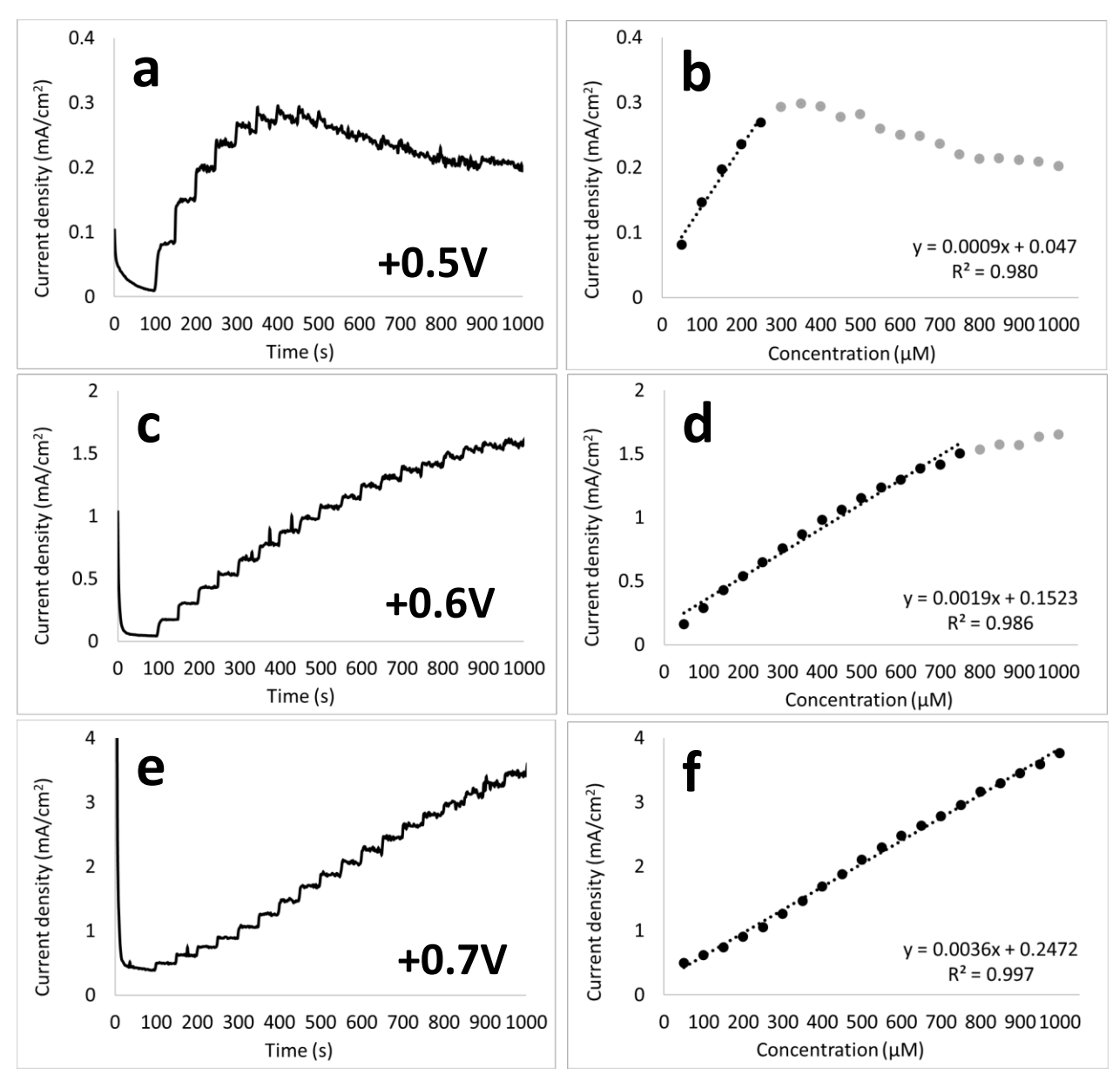


Figure 5. Amperometric responses at different potentials of (a) ± 0.5 V, (c) ± 0.6 V, and (e) ± 0.7 V with their corresponding calibration curves (b, d, and f, respectively) for the 60% Ni–TiO₂/XC72R electrode in 0.1 M NaOH for 50 μ M glucose aliquot additions every 50 s.

and 15.5 mM) had a mean salivary glucose level of 1.002 mg/dL (0.056 mM) and those with blood glucose levels between 180 and 440 mg/dL (10 mM and 24 mM) had a mean salivary glucose level of 2.31 mg/dL (0.13 mM).^[37] Therefore, the selected aliquots of 50 μ M adequately covered the salivary glucose level range for a noninvasive approach of the sensor. It is evident from Figure 5a, 5c, and 5e that increasing the potential leads to an increase in current. This enforces the idea that the applied potential directly affects the amperometric response of the enzyme–less biosensor. At a potential of +0.5V, a linear range exists from 50–250 μ M (R² = 0.98) with a sensitivity of 900 μ A mM⁻¹ cm⁻². When increasing the potential to +0.6V as seen in Figure 5c, the linear range expanded significantly to 750 μ M (R² = 0.99) and the sensitivity of the electrode increased to 1900 μ A mM⁻¹ cm⁻².

At the highest measured potential of +0.7V as shown in Figure 5f, the sensitivity of the electrode plot was enhanced to $3600~\mu A~mM^{-1}~cm^{-2}$, and the concentration range became linear from $0.05-1~mM~(R^2=0.99)$. The noise level at +0.7V also increases at higher glucose concentrations compared to +0.6V, which may be associated with more intermediate species adsorbed onto the catalyst surface. Given that the amperometric responses showed phenomenal sensitivity and linearity at low glucose concentrations, higher concentrations of 1 mM were used to replicate a concentration range analogous to human physiology. The Center for Disease Control and Prevention states that fasting blood sugar levels for a healthy individual are below 140 mg/dL (<8~mM), prediabetics are between 140–199 mg/dL (8-11~mM), and diabetics are anywhere above 200 mg/dL (>11.1~mM). Figure 6a displays the electrooxidation of glucose employing 1 mM (black line) and 50 μ M (red line) aliquots per step. As expected, higher currents are produced when increasing the aliquot concentrations from 50 μ M to 1 mM. The calibration curve for the 1 mM aliquots, shown in Figure 6b, generated a correlation of $R^2=0.99$, sensitivity of 273.7 μ A mM⁻¹

cm⁻², and detection limit of 3.13 μ M (S/N = 3) while that of the 50 μ M aliquot additions, shown in Figure 6c, produced a regression equation with correlation of R² = 0.99, sensitivity of 3300 μ A mM⁻¹ cm⁻², and detection limit of 144 nM (S/N = 3) at an applied potential of +0.7V. This demonstrates that the 60% Ni–TiO₂/XC72R electrode can effectively cover the glucose range found in human saliva (50–1000 μ M) and those in human blood systems (1–20 mM).

Interference studies.— Prior studies have demonstrated that the presence of chloride ions can interfere with the performance of non–enzymatic sensors. ^[19,20,38] Thus, amperometric studies were conducted using 0.1 M NaOH as the electrolyte while incorporating 0.1 M NaCl. Figure S9 displays the amperometric responses for the 60% Ni–TiO₂/XC72R electrode at +0.7V using

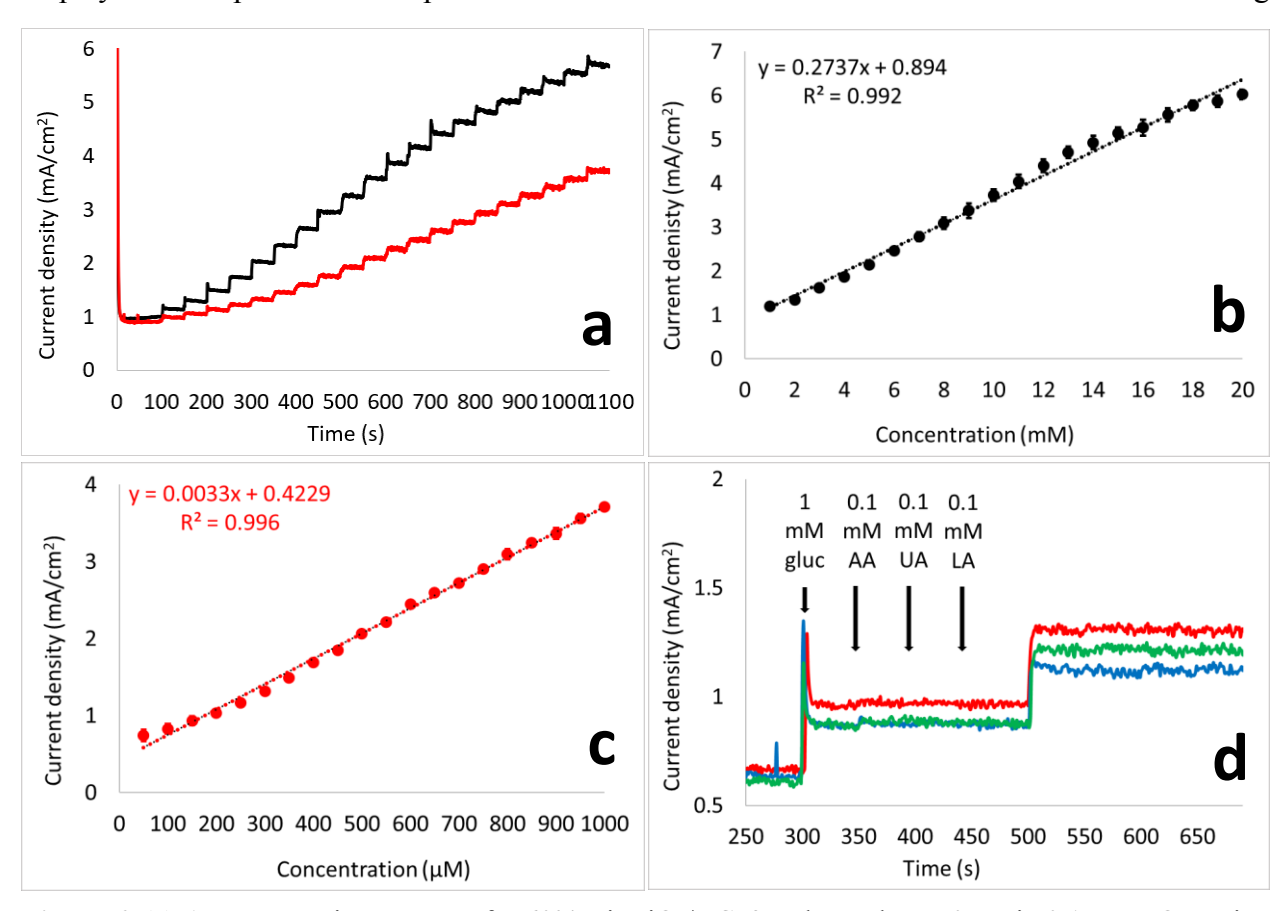


Figure 6. (a) Amperometric responses for 60% Ni–TiO₂/XC72R electrode at +0.7V in 0.1 M NaOH using 1 mM (black line) and 50 μ M (red line) aliquots per step and the (b and c, respectively) calibration curves with error bars (n = 3). (d) Three independent amperometric measurements for 60% Ni–TiO₂/XC72R electrode at +0.7V in 0.1 M NaOH using sequential aliquot additions of 1 mM glucose, 0.1 mM AA, 0.1 mM UA, and 0.1 mM LA.

glucose aliquots of 1 mM per step. Contrary to previous studies where a larger ionic activity would lead to the generation of higher currents, a minimal difference in current response was observed. Even though the sensitivity of the sensor increased to 287.7 µA mM⁻¹ cm⁻², there is not a significant difference between the electrolyte containing 0.1 M NaCl and that just containing 0.1 M NaOH. From these almost constant responses it can be concluded that the electrode is still active for glucose oxidation regardless of chloride ion presence. The presence of other analytes including uric acid (UA), lactic acid (LA), and ascorbic acid (AA) have been shown to directly interfere with the electrochemical oxidation of glucose, especially with nonenzymatic sensors. [19] Given that these compounds coexist with glucose in real blood samples, studies were performed to understand the selectivity of the new sensor towards glucose in the presence of these analytes. Figure 6d shows the amperometric responses of the 60% Ni–TiO₂/XC72R electrode at +0.7V in 0.1 M NaOH using sequential aliquots of 1 mM glucose, 0.1 mM AA, 0.1 mM UA, and 0.1 mM LA. It can be observed that these compounds do not produce a significant current response at this potential and thus, do not interfere with the electrochemical oxidation of glucose. The selectivity of the 60% Ni-TiO₂/XC72R in 0.1 M NaOH at +0.7V is exclusive to glucose.

Conclusion

This presented report showcased a convenient synthesis of a nickel–titania on carbon nanocomposite system for the amperometric electrooxidation of glucose. Varying wt. % of nickel precursor were reduced to Ni nanoparticles on a TiO_2 anatase / Vulcan carbon substrate by reduction with 35% hydrazine. The 60% (3:1) Ni– TiO_2 /XC72R nanocomposite was the most active towards glucose oxidation and thus studied as an enzyme–less, chronoamperometric glucose sensor. Using 50 μ M aliquots of glucose in 0.1 M NaOH alkaline medium at a potential of +0.7V (vs Hg/HgO), the sensor responded rapidly (< 3 s) providing a sensitivity of 3300 μ A mM⁻¹ cm⁻²

(n = 3) and detection limits of 144 nM (S/N = 3). Using aliquot concentrations of 1 mM glucose to mimic physiological blood conditions, the sensor continued to respond rapidly (< 1 s) showing a sensitivity of 273.7 μA mM⁻¹ cm⁻² (n = 3) and detection limits of 3.13 μM (S/N = 3). The nanocomposite is stable, has an anti–poisoning capacity by chloride ions, and is selective towards glucose amongst under analytes including 0.1 mM ascorbic acid, 0.1 mM uric acid, and 0.1 mM lactic acid. Results demonstrate that the 60% Ni–TiO₂/XC72R nanocomposite is an effective catalyst for glucose electrooxidation and a promising candidate for an enzyme–less sensor for glucose detection and monitoring.

Acknowledgement

Support of our work by the Loker Hydrocarbon Research Institute is gratefully acknowledged. The authors would also like to thank the National Science Foundation for funding (CHE–2018740) of the Rigaku Ultima IV X–ray Diffractometer.

References

- 1. E. W. Gregg, Y. J. Cheng, K. M. V. Narayan, T. J. Thompson, and D. F. Williamson, *Prev. Med. (Baltim).*, **45**, 348–352 (2007).
- 2. E. S. Ford, D. F. Williamson, and S. Liu, Am. J. Epidemiol., 146, 214–222 (1997).
- 3. P. Saeedi et al., *Global and regional diabetes prevalence estimates for 2019 and projections for 2030 and 2045 : Results from the International Diabetes Federation Diabetes Atlas*, *9 th edition*, p. 107843, Elsevier Ireland Ltd, (2019) https://doi.org/10.1016/j.diabres.2019.107843.
- 4. R. Muniyappa and S. Gubbi, Am. J. Physiol. Endocrinol. Metab., 318, E736–E741 (2020).
- 5. T. M. Dall et al., *Diabetes Care*, **37**, 3172–3179 (2014).
- 6. M. Adeel et al., Biosens. Bioelectron., 165, 112331 (2020) https://doi.org/10.1016/j.bios.2020.112331.
- 7. Y. Liu, M. Wang, F. Zhao, Z. Xu, and S. Dong, *Biosens. Bioelectron.*, 21, 984–988 (2005).
- 8. P. Mandpe, B. Prabhakar, H. Gupta, and P. Shende, Sens. Rev., 40, 497–511 (2020).
- 9. D. Chai et al., *Electrochim. Acta*, **189**, 295–302 (2016) http://dx.doi.org/10.1016/j.electacta.2015.12.071.
- 10. E. Mitsou, A. Xenakis, and M. Zoumpanioti, *Catalysts*, 7, 52 (2017).
- 11. Y. Wang et al., AMB Express, 8, 95 (2018) https://doi.org/10.1186/s13568-018-0618-z.

- 12. J. Zhao, F. Wang, J. Yu, and S. Hu, *Talanta*, 70, 449–454 (2006).
- 13. I. Danaee, M. Jafarian, F. Forouzandeh, F. Gobal, and M. G. Mahjani, *Electrochim. Acta*, **53**, 6602–6609 (2008).
- 14. Q. Yi and W. Yu, Microchim. Acta, 165, 381–386 (2009).
- 15. A. Habrioux et al., J. Phys. Chem. B, 111, 10329–10333 (2007).
- 16. Y. Zhao, X. Yang, J. Tian, F. Wang, and L. Zhan, *Int. J. Hydrogen Energy*, **35**, 3249–3257 (2010) http://dx.doi.org/10.1016/j.ijhydene.2010.01.112.
- 17. D. Basu and S. Basu, in *International Journal of Hydrogen Energy*,, vol. 37, p. 4678–4684, Elsevier Ltd (2012) http://dx.doi.org/10.1016/j.ijhydene.2011.04.158.
- 18. C. C. Chen, C. L. Lin, and L. C. Chen, *J. Power Sources*, **287**, 323–333 (2015) http://dx.doi.org/10.1016/j.jpowsour.2015.04.083.
- 19. Y. Ding et al., *Biosens. Bioelectron.*, **26**, 542–548 (2010) http://dx.doi.org/10.1016/j.bios.2010.07.050.
- 20. M. M. Rahman, A. J. S. Ahammad, J. H. Jin, S. J. Ahn, and J. J. Lee, Sensors, 10, 4855–4886 (2010).
- 21. G. Liu et al., *Talanta*, **101**, 24–31 (2012) http://dx.doi.org/10.1016/j.talanta.2012.08.040.
- 22. S. M. El-Refaei, M. M. Saleh, and M. I. Awad, *J. Power Sources*, **223**, 125–128 (2013) http://dx.doi.org/10.1016/j.jpowsour.2012.08.098.
- 23. K. K. Lee, P. Y. Loh, C. H. Sow, and W. S. Chin, *Electrochem. commun.*, **20**, 128–132 (2012) http://dx.doi.org/10.1016/j.elecom.2012.04.012.
- 24. L. C. Jiang and W. De Zhang, *Biosens. Bioelectron.*, **25**, 1402–1407 (2010).
- 25. K. E. Toghill, L. Xiao, M. A. Phillips, and R. G. Compton, *Sensors Actuators, B Chem.*, **147**, 642–652 (2010) http://dx.doi.org/10.1016/j.snb.2010.03.091.
- 26. J. Bai and B. Zhou, Chem. Rev., 114, 10131–10176 (2014).
- 27. Q. Yi, W. Huang, W. Yu, L. Li, and X. Liu, *Electroanalysis*, 20, 2016–2022 (2008).
- 28. C. Wang, L. Yin, L. Zhang, and R. Gao, J. Phys. Chem. C, 114, 4408–4413 (2010).
- 29. Y. Chen, J. Shen, and N. xian Chen, *Solid State Commun.*, **149**, 121–125 (2009) http://dx.doi.org/10.1016/j.ssc.2008.11.004.
- 30. E. Sanchez et al., J. Solid State Chem., 314, 309–314 (1996).
- 31. E. Cossar, M. S. E. Houache, Z. Zhang, and E. A. Baranova, *J. Electroanal. Chem.*, **870**, 114246 (2020) https://doi.org/10.1016/j.jelechem.2020.114246.
- 32. S. Chakrabarty et al., *J. Solid State Electrochem.*, **25**, 159–171 (2021).
- 33. H. Bode, K. Dehmelt, and J. Witte, *Electrochim. Acta*, 11, 1079–1087 (1966).
- 34. P. Oliva et al., *J. Power Sources*, **8**, 229–255 (1982).
- 35. R. S. Schrebler Guzmán, J. R. Vilche, and A. J. Arvía, J. Electrochem. Soc., 125, 1578–1587 (1978).
- 36. D. M. MacArthur, J. Electrochem. Soc., 117, 729 (1970).

- 37. V. Gupta and A. Kaur, J. Oral Maxillofac. Pathol., 24 (2020).
- 38. J. S. Ye et al., *Electrochem. commun.*, **6**, 66–70 (2004).